Nucleon charges and σ-terms in lattice QCD

C. Alexandrou,[1,2] S. Bacchio,[2] J. Finkenrath,[3] C. Iona,[1] G. Koutsou,[2] Y. Li,[1] and G. Spanoudes[1]

[1] *Department of Physics, University of Cyprus, P.O. Box 20537, 1678 Nicosia, Cyprus*
[2] *Computation-based Science and Technology Research Center, The Cyprus Institute, 20 Kavafi Str., Nicosia 2121, Cyprus*
[3] *Department of Theoretical Physics, European Organization for Nuclear Research, CERN, CH-1211 Geneva 23, Switzerland*

We determine the nucleon axial, scalar and tensor charges and the nucleon σ-terms using twisted mass fermions. We employ three ensembles with approximately equal physical volume of about 5.5 fm, three values of the lattice spacing, approximately 0.06 fm, 0.07 fm and 0.08 fm, and with the mass of the degenerate up and down, strange and charm quarks tuned to approximately their physical values. We compute both isovector and isoscalar charges and σ-terms and their flavor decomposition including the disconnected contributions. We use the Akaike Information Criterion to evaluate systematic errors due to excited states and the continuum extrapolation. For the nucleon isovector axial charge we find $g_A^{u-d} = 1.250(24)$, in agreement with the experimental value. Moreover, we extract the nucleon σ-terms and find for the light quark content $\sigma_{\pi N} = 41.9(8.1)$ MeV and for the strange $\sigma_s = 30(17)$ MeV.

Keywords: Nucleon charges, Nucleon Structure, Lattice QCD

arXiv:2412.01535v1 [hep-lat] 2 Dec 2024

I. INTRODUCTION

The nucleon axial, tensor and scalar charges, along with the σ-terms, are fundamental quantities within the Standard Model and provide insights into nucleon structure. The axial charge, g_A^{u-d}, determines the rate of neutron beta decay, providing a direct probe of chiral symmetry breaking in hadron physics. It also enters analyses of neutrinoless double-beta decay and plays a central role in tests of the unitarity of the Cabibbo-Kobayashi-Maskawa (CKM) matrix. Flavor-diagonal axial charges, g_A^f, describe the intrinsic spin, $\frac{1}{2}\Delta\Sigma_q$, carried by quarks in the nucleon and are measured in deep inelastic scattering (DIS) experiments at facilities such as Jefferson Lab and CERN, with future plans at the Electron-Ion Collider (EIC).

The isovector tensor and scalar charges, g_T^{u-d} and g_S^{u-d}, are less well known but are crucial in constraining beyond Standard Model (BSM) interactions [1]. These charges provide essential theoretical input for interpreting results from ongoing neutrino scattering experiments, such as DUNE [2], COHERENT [3], and GEMMA [4], as well as from direct dark matter detection searches [5–7]. Providing an accurate determination of the tensor charge is important for phenomenological analyses of the transvesity parton distribution function [8]. The nucleon σ-terms measure the contribution of quark masses to the nucleon mass, and enter in the determination of the elastic scattering cross section between dark matter candidates, such as weakly interacting massive particles (WIMPs).

In this work, we compute the nucleon charges and σ-terms, using twisted mass fermion ensembles at three different lattice spacings. These are simulated by the Extended Twisted Mass Collaboration (ETMC) using a mass degenerate up and down quark doublet, and the strange and charm quarks ($N_f = 2+1+1$) with all masses fixed to approximately their physical values, referred to as physical point. This allows for a precise determination of both isovector and flavor-diagonal charges, as well as the nucleon σ-terms, avoiding chiral extrapolations. Our results not only serve as a crucial benchmark for lattice QCD computations but also provide essential input for precision experiments aimed at probing BSM interactions, CP-violation, and dark matter detection.

II. METHODOLOGY

The nucleon axial, tensor, and scalar charges for each quark flavor f, denoted as $g^f_{\mathrm{A,T,S}}$, are derived from the nucleon matrix elements of the corresponding axial, tensor and scalar operators at zero momentum transfer. They are defined as

$$\langle N|\bar{\psi}^f \Gamma_{\mathrm{A,S,T}} \psi^f|N\rangle = g^f_{\mathrm{A,S,T}} \bar{u}_N \Gamma_{\mathrm{A,S,T}} u_N \,, \qquad (1)$$

where u_N is the nucleon spinor and $\Gamma_A = \gamma_\mu\gamma_5$ for the axial-vector, $\Gamma_S = \mathbb{1}$ for the scalar and $\Gamma_T = \sigma_{\mu\nu}$ for the tensor operators. The renormalization group invariant σ^f-term is defined by $m_f\langle N|\bar{\psi}_f\psi_f|N\rangle$, with m_f being the quark mass.

A. Gauge ensembles and statistics

To evaluate the nucleon matrix elements, we analyze gauge ensembles generated with the twisted-mass fermion discretization scheme, which inherently offers $\mathcal{O}(a)$-improvement [9, 10]. A clover term is included in the action [11], reducing isospin-breaking effects that arise from this fermion discretization.

The isosymmetric pion mass m_π =135 MeV [13, 14] is reproduced through the tuning of the bare light quark parameter μ_l. The parameters for the heavy quarks, μ_s and μ_c, are tuned by utilizing the kaon mass along with

Ensemble	Abrv.	V/a^4	β	a [fm]	m_π [MeV]
cB211.072.64	B64	$64^3 \times 128$	1.778	0.07957(13)	140.2(2)
cC211.060.80	C80	$80^3 \times 160$	1.836	0.06821(13)	136.7(2)
cD211.054.96	D96	$96^3 \times 192$	1.900	0.05692(12)	140.8(2)

TABLE I: Parameters of the $N_f = 2+1+1$ ensembles analyzed in this work. In the first column, we give the name of the ensemble, in the second the abbreviated name, in the third the lattice volume, in the fourth $\beta = 6/g^2$ with g the bare coupling constant, in the fifth the lattice spacing and in the last the pion mass. Lattice spacings and pion masses are taken from Ref. [12].

a properly defined ratio between the D-meson mass and its decay constant, as well as a phenomenologically motivated ratio between the strange and charm quark masses, following the approach of Ref. [13, 14]. The parameters of the ensembles used in this analysis are listed in Table I. The lattice spacings and pion masses are adopted from Ref. [12]. Lattice spacing values are determined in both the meson and nucleon sectors, and we report the values from the meson sector, which agree with those from the nucleon mass as found in Ref. [15].

cB211.072.64 749 configurations		
t_s/a	t_s [fm]	n_{src}
8	0.64	1
10	0.80	2
12	0.96	5
14	1.12	10
16	1.28	32
18	1.44	112
20	1.60	128
Nucleon 2pt n_{src}=477		

cC211.060.80 400 configurations		
t_s/a	t_s [fm]	n_{src}
6	0.41	1
8	0.55	2
10	0.69	4
12	0.82	10
14	0.96	22
16	1.10	48
18	1.24	45
20	1.37	116
22	1.51	246
Nucleon 2pt n_{src}=650		

cD211.054.96 494 configurations		
t_s/a	t_s [fm]	n_{src}
8	0.46	1
10	0.57	2
12	0.68	4
14	0.80	8
16	0.91	16
18	1.03	32
20	1.14	64
22	1.25	16
24	1.37	32
26	1.48	64
Nucleon 2pt n_{src}=480		

	cB211.072.64 749 configurations				**cC211.060.80** 400 configurations				**cD211.054.96** 494 configurations			
Flavour	N_{defl}	N_r	N_{Had}	N_{vect}	N_{defl}	N_r	N_{Had}	N_{vect}	N_{defl}	N_r	N_{Had}	N_{vect}
Light	200	1	512	6144	450	1	512	6144	0	8	512	49152
Strange	0	2	512	12288	0	4	512	24576	0	4	512	24576
Charm	0	12	32	4608	0	1	512	6144	0	1	512	6144

TABLE II: Statistics used for the connected two- and three-point functions (top) and disconnected loops (bottom). Top: In each table, we provide the sink-source time separations in lattice units (first column) and physical units (second column) and the number of source positions per configuration (third column). For each ensemble, the bottom row indicates the number of source positions used for the two-point functions. Bottom: For each ensemble, in the columns from left to right we give: i) the number of deflated eigenvectors N_{defl}, ii) the number of stochastic sources N_r, iii) the number of Hadamard vectors N_{Had}, and iv) the total number of computed vectors, N_{vect}, which after color and spin dilution are obtained via $12 \times N_r \times N_{Had}$.

To obtain the nucleon charges we evaluate two- and three-point nucleon correlation functions and carry out fits to isolate the ground state matrix element of interest as will be explained in detail in Sec. III A. In Table II, we present the statistics used for the calculation of the correlation functions, providing both the number of configurations analyzed and the number of source positions per configuration. The three-point functions are computed via the so-called *fixed sink* method, where we carry out a new inversion for each new sink-source separation. The number of source positions per configuration listed in Table II are increased with increasing separation so that the three-point function statistical errors are maintained roughly constant. Table II also includes details for the contributions from disconnected quark loops. These are calculated for the light, strange, and charm quark masses. To enhance the signal-to-noise ratio of these disconnected loops, several noise-reduction techniques are applied. These include the one-end trick [16], exact deflation of low modes [17], and hierarchical probing [18], as explained in Ref. [19] for the specific application to twisted mass fermions. The one-end trick is applied to all loops for all three ensembles. We also use hierarchical probing for the loops computed for all quark loops

with a probing distance of 8 for the light and strange quark loops and with 4 for the charm-quark loops. Deflation of low modes is applied to the light quark loops for the cB211.072.64 and cC211.060.80 ensembles. For the cD211.054.96 ensemble a higher number of stochastic sources are used since using deflation for this $96^3\times192$ lattice, which scales with the square of the volume, would be prohibitively expensive.

B. Computation of correlators

Extracting the nucleon matrix elements involves the computation of both three- and two-point Euclidean correlation functions. The two-point function reads

$$C(\Gamma_0,\vec{p};t_s)=\sum_{\vec{x}_s}e^{-i(\vec{x}_s)\cdot\vec{p}}\times \\ \mathrm{Tr}\left[\Gamma_0\left\langle\mathcal{J}_N(t_s,\vec{x}_s)\bar{\mathcal{J}}_N(0,\vec{0})\right\rangle\right], \tag{2}$$

where we set the source at the origin, t_s, x_s are the sink coordinates, Γ_0 is the unpolarized, positive parity projector $\Gamma_0=\frac{1}{2}(1+\gamma_0)$ and the interpolating field for the nucleon

$$\mathcal{J}_N(t,\vec{x})=\epsilon_{abc}u_a(x)\left(u_b^T(x)C\gamma_5 d_c(x)\right). \tag{3}$$

In order to increase the overlap of the interpolating field with the nucleon ground state and reduce contamination from excited states, so that the ground state dominates for as small time separations as possible, we apply *Gaussian smearing* [20, 21] to the quark fields entering the interpolating field

$$\widetilde{\psi}(\vec{x},t)=\sum_{\vec{y}}[1+a_G H(\vec{x},\vec{y};U(t))]^{N_G}\psi(\vec{y},t) \tag{4}$$

where ψ is either u or d of Eq. (3) and H is the hopping matrix

$$H(\vec{x},\vec{y};U(t))=\sum_{i=1}^{3}\left[U_i(x)\delta_{x,y-\hat{i}}+U_i^\dagger(x-\hat{i})\delta_{x,y+\hat{i}}\right]. \tag{5}$$

The parameters α_G and N_G are adjusted [22, 23] to achieve a nucleon smearing radius of approximately 0.5 fm. To suppress statistical noise arising from ultraviolet fluctuations, APE smearing [24] is applied to the gauge links used in the hopping matrix.

The three-point function for e.g. the axial-vector is given by

$$C^\mu(\Gamma_k,\vec{q},\vec{p'};t_s,t_{ins})=\sum_{\vec{x}_s,\vec{x}_{ins}}e^{i\vec{x}_{ins}\cdot\vec{q}}e^{-i\vec{x}_s\cdot\vec{p'}}\times \\ \mathrm{Tr}\left[\Gamma_k\left\langle\mathcal{J}_N(t_s,\vec{x}_s)\mathcal{O}^\mu(t_{ins},\vec{x}_{ins})\bar{\mathcal{J}}_N(0,\vec{0})\right\rangle\right], \tag{6}$$

where $\Gamma_k=i\Gamma_0\gamma_5\gamma_k$ is the polarized projector, $\mathcal{O}^\mu=\bar{\psi}\gamma_\mu\gamma_5\psi$ is the axial operator insertion, $\vec{p'}$ is the sink momentum and $\vec{q}$ is the insertion momentum.

For the charges and σ-terms, we use $\vec{q}=0$ restricting to the forward limit and to nucleons with no momentum boost, i.e. $\vec{p'}=0$. Similar expressions hold for the scalar and the tensor three-point functions, with operator insertion $\mathcal{O}=\bar{\psi}\psi$ and $\mathcal{O}^{\mu\nu}=\bar{\psi}\sigma^{\mu\nu}\psi$, respectively. The scalar matrix elements are extracted using the unpolarized projector Γ_0, while the tensor requires the polarized, Γ_k. In what follows we will use the notation for the axial-vector, keeping in mind the straight forward generalization to the scalar and tensor operator insertions.

III. ANALYSIS OF CORRELATORS

The spectral decomposition of the two- and three-point functions are given respectively by

$$C(\Gamma_0,\vec{p};t_s)=\sum_i^\infty c_i(\vec{p})e^{-E_i(\vec{p})t_s}\quad\text{and} \tag{7}$$

$$C^\mu(\Gamma_k,\vec{q};t_s,t_{ins})=\sum_{i,j}^\infty A_\mu^{i,j}(\Gamma_k,\vec{q})e^{-E_i(\vec{0})(t_s-t_{ins})-E_j(\vec{q})t_{ins}}. \tag{8}$$

The coefficients c_i of the two-point function are overlap terms given by

$$c_i(\vec{p})=\mathrm{Tr}[\Gamma_0\left\langle\mathcal{J}_N|N_i(\vec{p})\right\rangle\left\langle N_i(\vec{p})|\bar{\mathcal{J}}_N\right\rangle] \tag{9}$$

and the coefficients $A_\mu^{i,j}(\Gamma_k,\vec{q})$ in the three-point function are given by

$$A_\mu^{i,j}(\Gamma_k,\vec{q})=\mathrm{Tr}[\Gamma_k\left\langle\mathcal{J}_N|N_i(\vec{0})\right\rangle\left\langle N_i(\vec{0})|\mathcal{O}^\mu|N_j(\vec{q})\right\rangle \\ \left\langle N_j(\vec{q})|\bar{\mathcal{J}}_N\right\rangle], \tag{10}$$

where $\langle N_i(\vec{0})|\mathcal{O}^\mu|N_j(\vec{0})\rangle$ is the matrix element of interest for the axial case, and similarly the scalar and tensor three-point functions give coefficients $A^{i,j}(\Gamma_0,\vec{q})$ and $A_{\mu\nu}^{i,j}(\Gamma_k,\vec{q})$, respectively. The overlaps between the interpolating field and the nucleon state $|N\rangle$, such as $\langle\Omega|\mathcal{J}_N|N\rangle\equiv\langle\mathcal{J}_N|N\rangle$, need to be canceled in order for us to access the matrix element. In order to cancel these unknown overlaps, we construct the ratio of the three- to two-point function

$$R_A^\mu(\Gamma_k;t_s,t_{ins})=\frac{C^\mu(\Gamma_k,\vec{0};t_s,t_{ins})}{C(\Gamma_0,\vec{0};t_s)}, \tag{11}$$

i.e. setting $\vec{q}=\vec{0}$ in the three-point and $\vec{p}=\vec{0}$ in the two-point functions. In the limit of large time separations $\Delta E(t_s-t_{ins})\gg1$ and $\Delta E t_{ins}\gg1$, with ΔE being the energy difference between the first excited state and ground state, the ratio gives us the desired axial charge

$$R_A^k(\Gamma_k;t_s,t_{ins})\to g_A, \tag{12}$$

and similarly R_S and $R_T^{\mu\nu}$ yield the scalar (g_S) and tensor (g_T) charge respectively. Thus we use the parameters c_0

and $A^{0,0}$ extracted from our data and substitute Eqs. (7) and (8) into Eq. (11) to obtain the charges via

$$g_S = Z_P \frac{A^{0,0}(\Gamma_0, \vec{0})}{c_0(\vec{0})},$$
$$g_A = Z_A \frac{A_k^{0,0}(\Gamma_k, \vec{0})}{c_0(\vec{0})},$$
$$g_T = Z_T \epsilon^{ijk} \frac{A_{ij}^{0,0}(\Gamma_k, \vec{0})}{c_0(\vec{0})}, \quad (13)$$

where Z_P, Z_A, and Z_T, are renormalization constants that will be discussed in Sec. IV. In practice, we need to identify the smallest possible t_s and t_{ins} for which excited state contributions are sufficiently suppressed. How fast ground state dominance is achieved depends on the smearing procedure applied on the interpolating fields and the energy gap between the ground state and the excited states. Additionally, noise increases exponentially with t_s, so establishing convergence to the ground state as early as possible is essential. We will employ a fitting strategy of multi-state analysis of the contribution of the first $N_{st} - 1$ excited states. This aims to reliably determine the values of c_0 and $A^{0,0}$ and is described in Sec. III A.

A. Fitting Strategy

To extract the ground state matrix elements, we perform simultaneous fits to the two-point functions with the highest statistics and the ratio of Eq. (11). To construct the ratio we divide the three-point function with the two-point function having the same statistics to take advantage of the correlations between them.

Since the optimal fit ranges in t_s and t_{ins} may vary for each case, we explore a wide parameter space in the fitting ranges. In detail, we perform multiple fits by varying the following parameters:

- $\boldsymbol{N_{st}}$: We truncate the sums over the energy states contributing to the two- (7) and three-point (8) functions to a maximum of $i_{max} = N_{st} - 1$ with $N_{st} = 2$. We call these *two-state* fits. If there is no detectable contamination due to excited states in the ratio, we fit it to a constant, performing a *plateau* ($N_{st} = 1$) fit.
- $\boldsymbol{t_{2pt}^{low}}$: We vary the lower time, t_{2pt}^{low}, in the fitting of the two-point functions, seeking for a region where only two states dominate.
- $\boldsymbol{t_s^{low}}$: Similarly, we vary the smallest value of the sink time t_s, we use for the fitting of the ratio and fit to all $t_s \geq t_s^{low}$ available.
- $\boldsymbol{t_{ins,0}, t_{ins,s}}$: We vary the number of insertion time slices from the source and the sink times that we keep in the fits to the ratio. We use $t_{ins} \in [t_{ins,0}, t_s - t_{ins,s}]$. For the charges we have $\vec{q} = 0$ so we fix $t_{ins,0} = t_{ins,s}$.

B. Model Average

From each combination of the varied parameters, we obtain a different result. We average the results using the *Akaike Information Criterion (AIC)* [25, 26]. In summary, for each fit i, we associate a weight w_i, which we define as

$$\log(w_i) = -\frac{\chi_i^2}{2} + N_{\mathrm{dof},i}, \quad (14)$$

where $N_{\mathrm{dof}} = N_{\mathrm{data}} - N_{\mathrm{params}}$ is the number of degrees of freedom for each fit. We then use the weights to define the probability

$$p_i = \frac{w_i}{Z} \quad \text{with} \quad Z = \sum_i w_i. \quad (15)$$

The *Model Average (MA)* value of an observable $\mathcal{O}$ is given as

$$\langle \mathcal{O} \rangle_{MA} = \sum_i \bar{\mathcal{O}}_i p_i \quad \text{with} \quad \sigma_{MA}^2 = \sum_i (\sigma_i^2 + \bar{\mathcal{O}}_i^2) p_i - \langle \mathcal{O} \rangle_{MA}^2 \quad (16)$$

with $\bar{\mathcal{O}}_i$ and σ_i being the central value and error of the observable resulting from the i_{th} fit.

IV. RENORMALIZATION

Matrix elements computed in lattice QCD need to be renormalized in order to relate to physical observables. In the physical basis of the twisted-mass formulation, we use the renormalization functions Z_A for the renormalization of the axial-vector current, Z_P for the scalar and Z_T for the tensor. We compute both flavor singlet and nonsinglet renormalization factors for isoscalar and isovector combinations, respectively. We use gauge ensembles simulated specifically for the renormalization program with four mass degenerate quarks ($N_f = 4$) at the same β values as the three physical point ensembles used in the analysis of the matrix elements. For each β, we employ four ensembles of different sea quark masses to perform chiral extrapolations. We list these ensembles in Table III.

The renormalization factors are calculated nonperturbatively by employing the RI′/MOM scheme [27] followed by perturbative conversion to $\overline{\mathrm{MS}}$ at the scale $\bar{\mu} = 2$ GeV. The RI′/MOM condition for the quark bilinear operators is

$$(Z_q^{\mathrm{RI}'})^{-1} Z_\Gamma^{\mathrm{RI}'} \frac{1}{12} \mathrm{Tr}[\Lambda_\Gamma(p)(\Lambda_\Gamma^{\mathrm{tree}}(p))^{-1}]|_{p^2=\mu_0^2} = 1, \quad (17)$$

where $\Lambda_\Gamma(p)$ is the amputated vertex function of the bilinear operator with external quark fields, and $\Lambda_\Gamma^{\mathrm{tree}}$ is

Ensemble	β	$L^3 \times T$	$a\mu_{\rm sea}$	κ	$c_{\rm SW}$
cB4.060.24	1.778	$24^3 \times 48$	0.0060	0.139305	1.6900
cB4.075.24	1.778	$24^3 \times 48$	0.0075	0.139308	1.6900
cB4.088.24	1.778	$24^3 \times 48$	0.0088	0.139310	1.6900
cB4.100.24	1.778	$24^3 \times 48$	0.0100	0.139312	1.6900
cC4.050.32	1.836	$32^3 \times 64$	0.0050	0.1386735	1.6452
cC4.065.32	1.836	$32^3 \times 64$	0.0065	0.1386740	1.6452
cC4.080.32	1.836	$32^3 \times 64$	0.0080	0.1386745	1.6452
cC4.095.32	1.836	$32^3 \times 64$	0.0095	0.1386760	1.6452
cD4.040.48	1.900	$48^3 \times 96$	0.0040	0.13793128	1.6112
cD4.050.48	1.900	$48^3 \times 96$	0.0050	0.13793128	1.6112
cD4.065.48	1.900	$48^3 \times 96$	0.0065	0.13793128	1.6112
cD4.080.48	1.900	$48^3 \times 96$	0.0080	0.13793128	1.6112

TABLE III: $N_f = 4$ gauge ensembles used for the computation of the renormalization functions. In the first column we give their name, in the second $\beta = (2N/g^2)$, in the third the lattice volume ($L^3 \times T$) in units of a, in the fourth the twisted-mass parameter ($a\mu$), in the fifth the hopping parameter κ and in the last the clover coefficient $c_{\rm SW}$.

the corresponding tree-level value. $Z_q^{\rm RI'}$ is the renormalization factor of the quark field calculated using the following condition

$$Z_q^{\rm RI'} = \frac{1}{12}{\rm Tr}[S^{-1}(p)S^{\rm tree}(p)] = 1, \qquad (18)$$

where $S(p)$ ($S^{\rm tree}(p)$) is the lattice (tree-level) quark propagator. The trace and the inverse in the above condition is taken over spin and color indices. The momentum p of the vertex function and quark propagator is set to the renormalization scale μ_0 of the RI$'$/MOM scheme.

We employ the momentum source approach [28], in which the vertex functions are calculated with a momentum-dependent source. This method requires separate inversions for each value of the renormalization scale, but has the advantage of high statistical accuracy and the evaluation of the vertex for any operator at negligible computational cost. For the singlet operators, the vertex functions have an additional disconnected contribution, which is calculated using the same methods described in Sec. II A, i.e. the one-end trick [16] and hierarchical probing [18].

The RI$'$ condition is defined for zero quark masses. To eliminate the mass contributions in the vertex functions, we perform chiral extrapolations using the set of ensembles in Table III for each β value. For Z_A and Z_T, a linear fit with respect to the twisted-mass parameter $\mu_{\rm sea}$ is employed, given by

$$Z_\Gamma(\mu_0, \mu_{\rm sea}) = c_0(\mu_0) + c_1(\mu_0) \cdot (a\mu_{\rm sea}),$$

which is sufficient for removing the mild dependence on the quark mass, as observed in similar investigations, e.g., in Ref. [29]. The pseudoscalar vertex function suffers from a pion pole and a dedicated analysis is needed to remove it reliably. We follow the procedure described in Ref. [15], where a non-unitary prescription is employed, in which the values of sea and valence quark masses are not equal. The pseudoscalar vertex functions are calculated for multiple values of the valence quark mass for each sea quark mass and a double chiral extrapolation is performed (see Ref. [15] for more details).

To reduce systematic errors related to lattice artifacts and rotational $O(4)$ breaking effects, we employ spatially isotropic momenta of the form

$$(ap) \equiv 2\pi[(n_t{+}0.5)/(T/a), n_x/(L/a), n_x/(L/a), n_x/(L/a)],$$

where $n_i \in \mathbb{Z}$, L (T) is the spatial (temporal) extend of the lattice, and we employ the momentum cuts given by $\sum_i p_i^4/(\sum_i p_i^2)^2 < 0.3$. The momentum form respects the periodic (antiperiodic) boundary conditions applied on the quark fields at a spatial (temporal) direction. Also, an important aspect of our renormalization program is the improvement of the nonperturbative estimates by subtracting one-loop discretization errors, calculated in lattice perturbation theory. This procedure results in a milder dependence of the renormalization factors on (a^2p^2). Further details can be found in similar investigations of our group, see, e.g., Ref. [29].

After chiral extrapolation and subtraction of one-loop artifacts, we evolve the resulting values of the RI$'$/MOM renormalization factors at a large reference momentum scale $\mu_{\rm ref}$ using continuum perturbation theory:[1]

$$Z_\Gamma^{\rm RI'}(\mu_{\rm ref}^2, \mu_0^2) \;=\; Z_\Gamma^{\rm RI'}(\mu_0^2)\, \frac{R_\Gamma^{\rm RI'}(a_s(\mu_{\rm ref}^2))}{R_\Gamma^{\rm RI'}(a_s(\mu_0^2))}, \qquad (19)$$

$$R_\Gamma^X(x) \;=\; \exp\Big\{ \int^x dx' \frac{\gamma_\Gamma^X(x')}{\beta^X(x')} \Big\} \qquad (20)$$

where $\gamma_\Gamma^X(a_s)$ is the anomalous dimension of the operator being considered and $\beta^X(a_s)$ the β function, within the scheme X. Note that the evolution of the scale is not applied in the nonsinglet axial-vector operator because it has zero anomalous dimension. In contrast, the singlet axial current has a nonzero anomalous dimension due to the axial anomaly [34]. Then, we apply a linear fit in μ_0^2 to eliminate residual dependence on the initial scale μ_0^2, of the form

$$Z_\Gamma(\mu_{\rm ref}^2, \mu_0^2) = c_0(\mu_{\rm ref}^2) + c_1(\mu_{\rm ref}^2) \cdot \mu_0^2.$$

In Fig. 1, we provide the momentum fits for both singlet and nonsinglet renormalization factors $Z_P^{s(ns)}$, $Z_A^{s(ns)}$ and $Z_T^{s(ns)}$, for the three lattice spacings, using a reference scale of $\mu_{\rm ref}^2 = 21{\rm GeV}^2$. The fit range is set to

[1] The anomalous dimensions of the operators in RI$'$/MOM is known to 4 loops for nonsinglet operators [30–32] and to 2 loops for singlet operators [33].

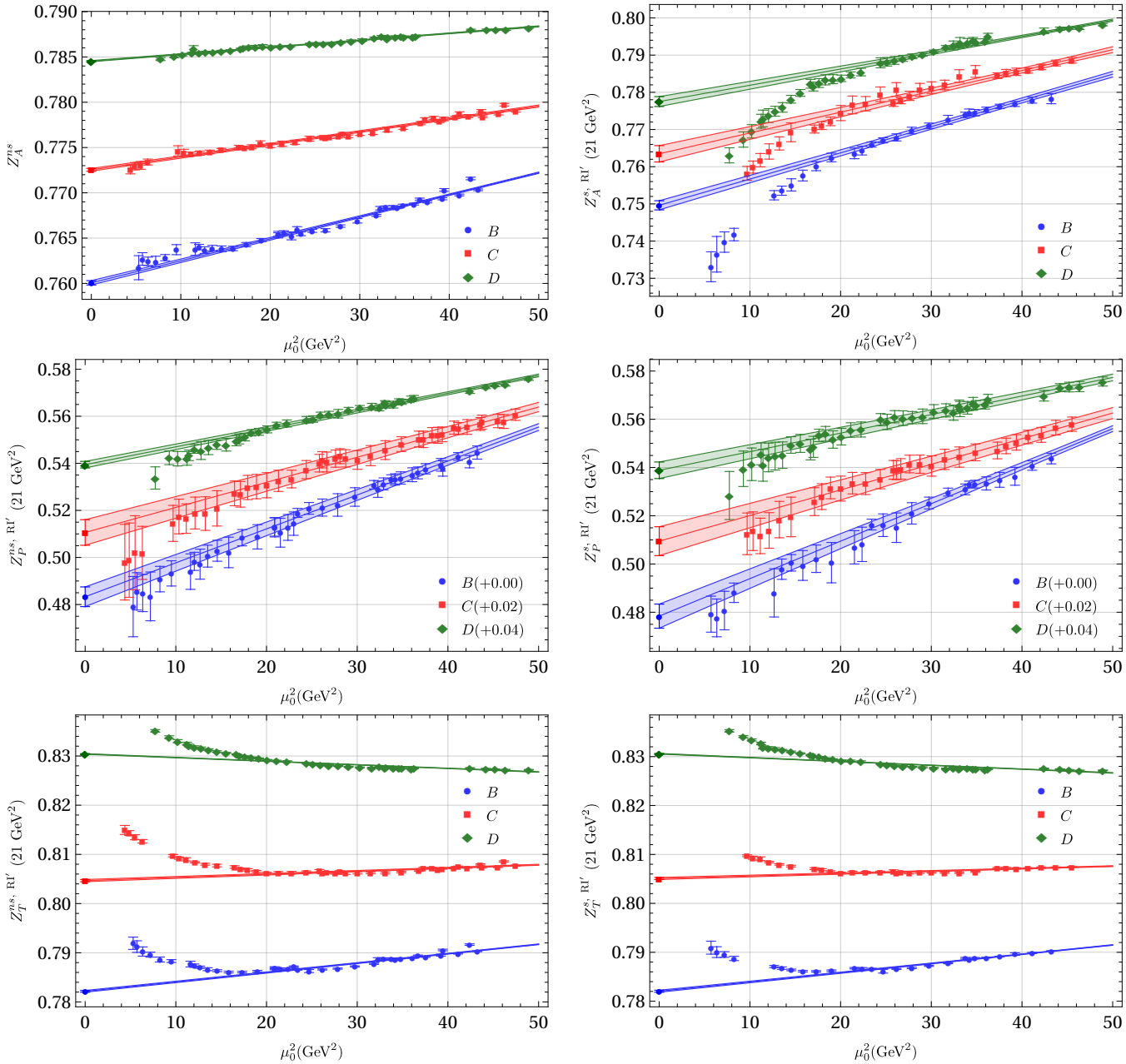

FIG. 1: Renormalization functions in RI′/MOM scheme at 21 GeV^2

12 GeV^2 - 50 GeV^2 for $Z_P^{s(ns)}$ and Z_A^{ns}, and 18 GeV^2 - 50 GeV^2 for Z_A^s and $Z_T^{s(ns)}$. In these ranges, the linear fit can sufficiently describe the residual momentum dependence. Lower momenta are excluded from the fits, where large nonperturbative effects (e.g., hadronic contaminations) are present and in which perturbative conversion does not work properly.

The extrapolated values of the renormalization factors at $\mu_0^2 = 0$ are converted to the $\overline{\mathrm{MS}}$ scheme at the reference scale of 2 GeV, using an intermediate Renormalization Group Invariant (RGI) scheme given by

$$Z_\Gamma^{\overline{\mathrm{MS}}}(4\mathrm{GeV}^2) = C_\Gamma^{\overline{\mathrm{MS}},\mathrm{RI}'}(4\mathrm{GeV}^2, 21\mathrm{GeV}^2) \cdot Z_\Gamma^{\mathrm{RI}'}(21\mathrm{GeV}^2), \tag{21}$$

where $C_\Gamma^{\overline{\mathrm{MS}},\mathrm{RI}'}$ is calculated up to four loops (two loops) in perturbation theory for the nonsinglet (singlet) operators [30–33]. The final values for the renormalization factors of the quark bilinears under study in the $\overline{\mathrm{MS}}$ scheme and at 2 GeV are given in Table IV. The error quoted in the parenthesis is the total error by adding in quadrature the statistical and systematic errors. The systematic error is estimated by varying the fit intervals in the

momentum fits, as well as, by varying the highest perturbative order that we include in the analytical expression of evolution and conversion functions.

	B64	C80	D96
Z_A^{ns}	0.7598(8)	0.7724(4)	0.7849(2)
Z_A^{s}	0.7740(120)	0.7921(84)	0.8030(91)
Z_P^{ns}	0.4695(45)	0.4771(55)	0.4841(32)
Z_P^{s}	0.4638(61)	0.4767(61)	0.4845(39)
Z_T^{ns}	0.8314(9)	0.8516(33)	0.8756(12)
Z_T^{s}	0.8293(27)	0.8493(41)	0.8763(29)

TABLE IV: Renormalization factors for the singlet (s) and nonsinglet (ns) operators in the $\overline{\text{MS}}$ scheme at 2 GeV.

V. RESULTS

A. Nucleon charges

The analysis carried out for the extraction of the nucleon ground state matrix element for the axial charges is shown in Figs. 2, 3 and 4 for the three ensembles analyzed here. As mentioned previously, we obtain the desired charge from the matrix element of the appropriate current at zero momentum transfer. For example, the isovector axial charge is obtained by computing the three-point function of the axial-vector operator given by

$$\mathcal{O}_A^{u-d} \equiv A_\mu = \bar{u}\gamma_\mu\gamma_5 u - \bar{d}\gamma_\mu\gamma_5 d, \tag{22}$$

where u and d are the up and down quark fields respectively.

As can be seen in Figs. 2, 3, and 4, the ratios of the connected contributions, from which the isovector and isoscalar combinations are determined, exhibit a considerable dependence on t_{ins} which indicates sizeable excited state contributions. For these cases we therefore perform 2-state fits, following the fitting approach of Sec. III A, with $N_{st} = 2$. Furthermore, for the isovector case, we include in the fit the temporal component of the three-point function with one unit of momentum transfer, $C^0(\Gamma_k, \frac{2\pi}{L}\hat{k}; t_s, t_{ins})$, where L is the spatial length of the lattice and $\hat{k}$ a unit vector in the k spatial direction, and correspondingly the two-point function with one unit of momentum. This analysis is motivated by chiral perturbation theory [35, 36] which foresees an amplification of the axial matrix element between a nucleon and pion-nucleon state, i.e. the $A_\mu^{0,1}$ and $A_\mu^{1,0}$ coefficients. The temporal component of the axial operator is obtained at no additional computational cost in our setup and since it exhibits strong dependence on the excited state can be used for a more precise identification of the πN energy and thus a better estimation of the ground-state matrix element of interest.

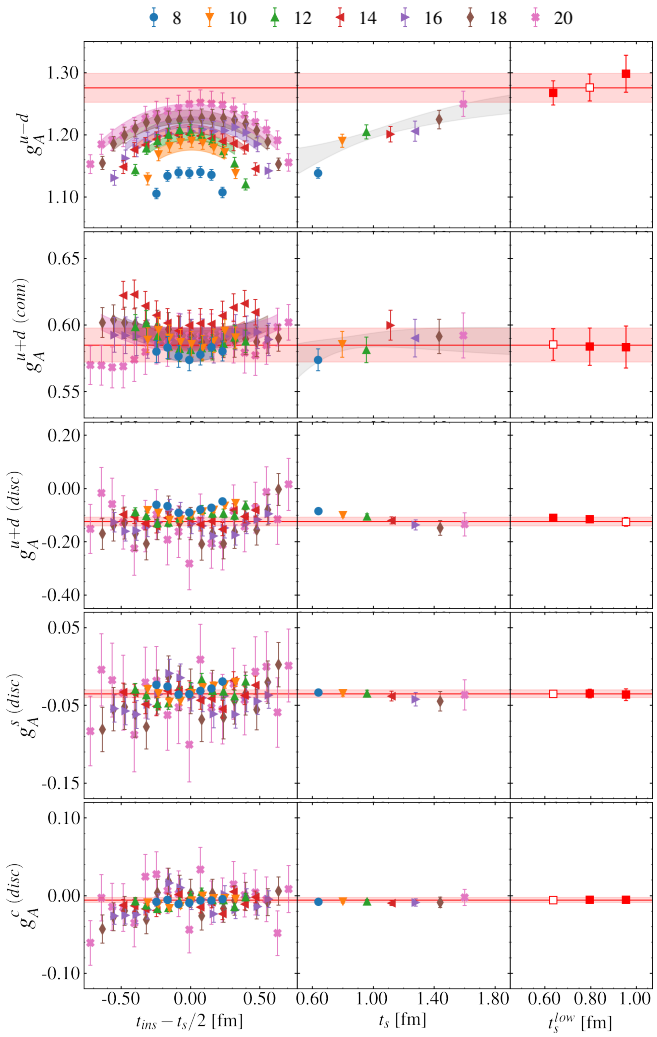

FIG. 2: Extraction of the isovector (first row), isoscalar connected (second row), isoscalar disconnected (third row), strange (fourth row), and charm (fifth row) contributions to the axial charge, for the B64 ensemble. In the first column, we show the ratios versus $t_{ins} - t_s/2$ with the symbol notation for each value of t_s given in the legend. The horizontal bands that span all columns are the model averaged results. In the middle column, we show the ratio versus t_s for $t_{ins} = t_s/2$ when 2-state fits are performed (i.e. for the connected contributions) or the result of a constant fit on each t_s separately when plateau fits are performed (i.e. for the disconnected contributions). When 2-state fits are performed, we also plot a gray band that shows the resulting ratio dependence on t_s for $t_{ins} = t_s/2$ as predicted by the fit. In the last column, we show the value of the fit with the largest weight for a fixed t_s^{low}, as explained in the text. The open symbol shows the t_s^{low} with the largest weight. We note that for the disconnected data, odd source-sink separations are also used in the analysis, that are not plotted here for better visibility.

For the disconnected contributions shown in Figs. 2, 3, and 4, namely the isoscalar g_A^{u+d} and the single-flavor g_A^s and g_A^c, we observe no detectable excited state contamination within the accuracy of our results and we thus use plateau fits for these quantities. We note that for the disconnected contributions, obtained by combining

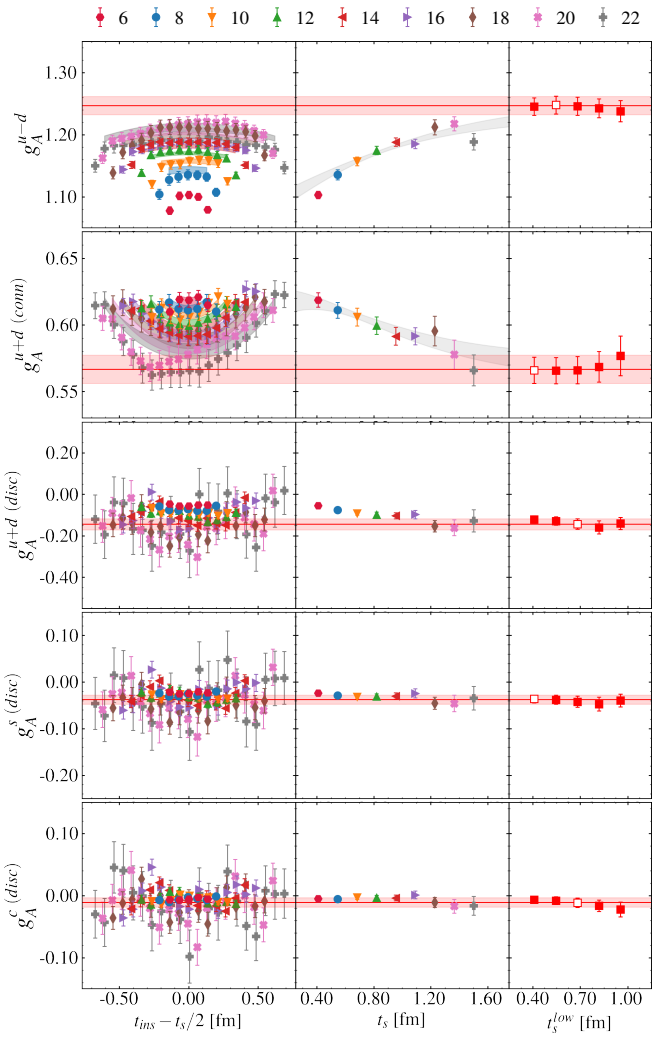

FIG. 3: Extraction of the axial charges for the C80 ensemble. The notation is the same as in Fig. 2.

the fermion loop with the two-point function, and thus in principle have all values of t_s available, we choose to plot even values of t_s for clarity and to match those of the connected contributions (see Table II), where the values of t_s need to be chosen beforehand within the fixed sink approach employed here.

The maximum value of t_s^{low} is taken to be approximately the same in physical units (fm) for the three ensembles considered. This corresponds to $t_s^{low}/a = 12$, 14 and 16 or $t_s^{low} = 0.96, 0.96$ and 0.91 fm for the B64, C80 and D96 ensembles, respectively. For all three ensembles, we observe a very mild dependence on t_s^{low}. The results in the right columns of Figs. 2, 3 and 4, correspond to the highest probability model for each value of t_s^{low}, when varying $t_{ins,0}$ and t_{2pt}^{low}. Namely, depending on the ensemble and quantity analyzed, for the connected contributions where we perform 2-state fits, $t_{ins,0}$ varies from $\sim$0.06 fm to $\sim$0.16 fm and t_{2pt}^{low} varies from $\sim$0.34 fm to $\sim$0.72 fm, while for the disconnected, where we fit to a constant, $t_{ins,0}$ varies from $\sim$0.17 fm to $\sim$0.40 fm.

We take the continuum limit, $a \to 0$, using the results from the three available ensembles with different lattice spacings. We carry out three types of extrapolation and evaluate a combined systematic and statistical error via a model average over the three fits. Namely, we use a linear fit in a^2 and a constant fit either using all three ensembles or when omitting the coarser ensemble, B64. A strong dependence on the lattice spacing will result in a model average favoring the linear fit, while a mild a^2 dependence will lead to a model average favoring the two constant fits.

The continuum limit extrapolations for the isovector, isoscalar, the strange and charm axial charges are shown in Fig. 5. The isoscalar combination includes the disconnected contributions. In Table V, we give our results for each gauge ensemble as well as our final continuum limit extrapolated results.

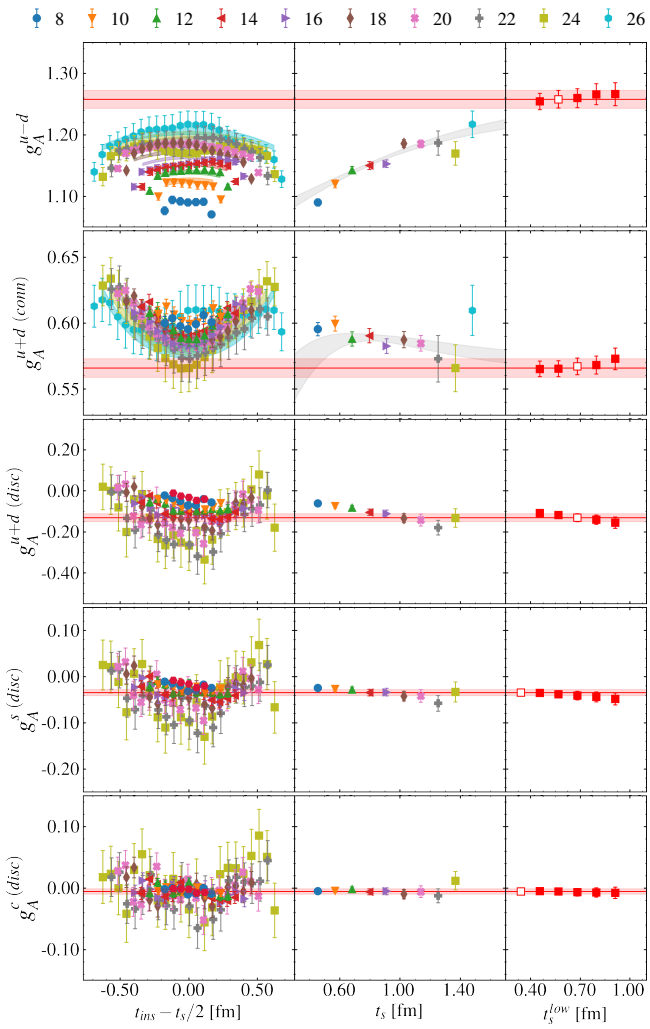

FIG. 4: Extraction of the axial charges for the D96 ensemble. The notation is the same as in Fig. 2.

We perform the same analysis for the scalar charges as we did for the axial. In absence of any insight similar to the axial case for the dependence on excited states, we restrict to using ratios and two-point functions at zero momentum. The ratios and extracted values are shown in

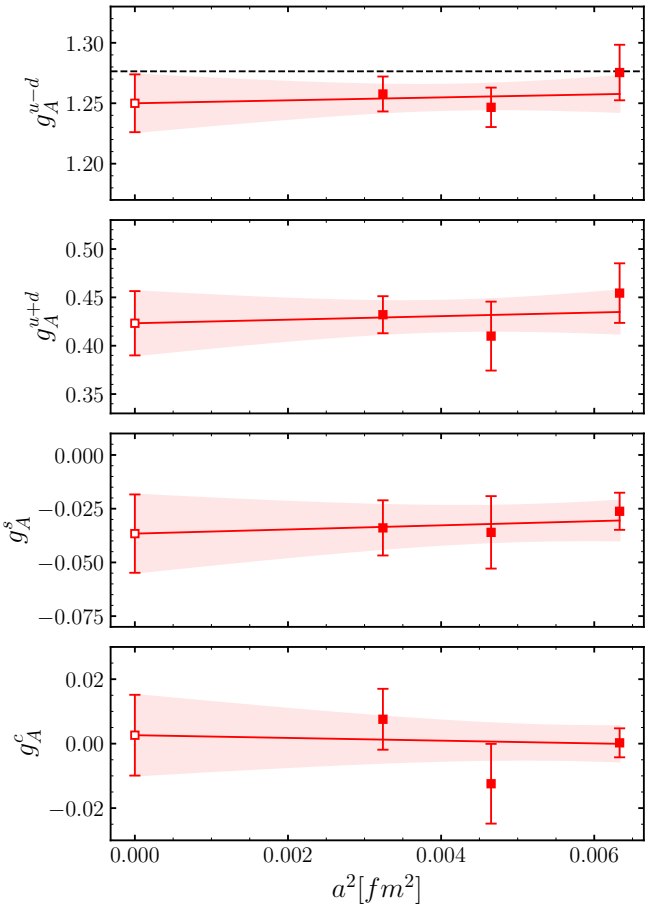

FIG. 5: Continuum limit of the nucleon axial charges (open symbols and band) extrapolated from three values of a (filled symbols). The extrapolation is the result of a model average which combines linear and constant fits as explained in the text. For the isovector g_A^{u-d}, the dashed line represents the experimental value [37].

g_A	$u-d$	$u+d$	$u+d-2s$	$u+d+s-3c$	$u+d+s+c$
B64	1.275(23)	0.454(31)	0.511(22)	0.432(20)	0.433(30)
C80	1.247(16)	0.410(36)	0.489(28)	0.418(23)	0.368(65)
D96	1.258(14)	0.432(19)	0.4952(95)	0.371(21)	0.401(49)
$a=0$	1.250(24)	0.423(33)	0.490(20)	0.343(55)	0.382(70)

g_A	u	d	s	c
B64	0.867(18)	-0.408(14)	-0.0262(86)	0.0003(45)
C80	0.832(22)	-0.415(21)	-0.036(17)	-0.012(12)
D96	0.843(16)	-0.415(15)	-0.034(13)	0.0076(94)
$a=0$	0.832(28)	-0.417(22)	-0.037(18)	0.003(13)

TABLE V: Values for the axial 2-, 3-, and 4-flavor isovector and isoscalar combinations (top) and the extracted single flavor charges (bottom) for each ensemble and in the continuum limit, using the model average strategy described in the text.

Figs. 6, 7 and 8 for the three ensembles. Here we observe excited state contamination and thus employ 2-state fits in all contributions apart from the disconnected ratios yielding g_S^c. We also observe a larger relative uncertainty for these quantities. The continuum limit is taken in the same way as for the axial charges and our final results are presented in Fig. 9 and in Table VI.

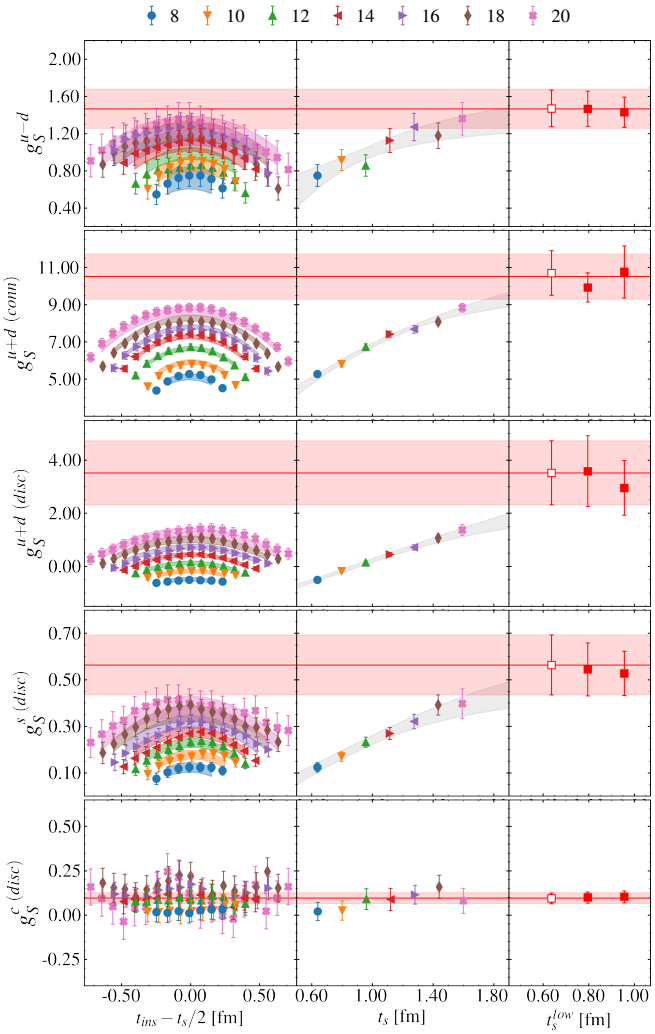

FIG. 6: The ratio and fit results for the B64 ensemble for scalar charges. The notation is the same as in Fig. 2, with 2-state fits being used for all cases except for g_S^c, where we use constant fits.

g_S	$u-d$	$u+d$	$u+d-2s$	$u+d+s-3c$	$u+d+s+c$
B64	1.47(23)	13.4(1.9)	11.8(1.8)	12.6(1.9)	13.9(1.9)
C80	1.35(21)	12.3(1.3)	11.9(1.4)	12.2(1.3)	12.4(1.2)
D96	1.18(13)	11.9(1.2)	11.2(1.4)	11.5(1.2)	12.7(1.4)
$a=0$	1.08(31)	11.5(2.2)	11.2(2.1)	11.4(2.1)	12.2(2.2)

g_S	u	d	s	c
B64	7.23(97)	5.76(85)	0.58(18)	0.32(21)
C80	6.78(68)	5.43(59)	0.17(18)	0.05(11)
D96	6.59(67)	5.41(62)	0.42(28)	0.29(21)
$a=0$	6.4(1.1)	5.30(98)	0.16(37)	0.09(26)

TABLE VI: Values for the scalar 2-, 3-, and 4-flavor isovector and isoscalar combinations (top) and the extracted single flavor charges (bottom) for each ensemble and in the continuum limit.

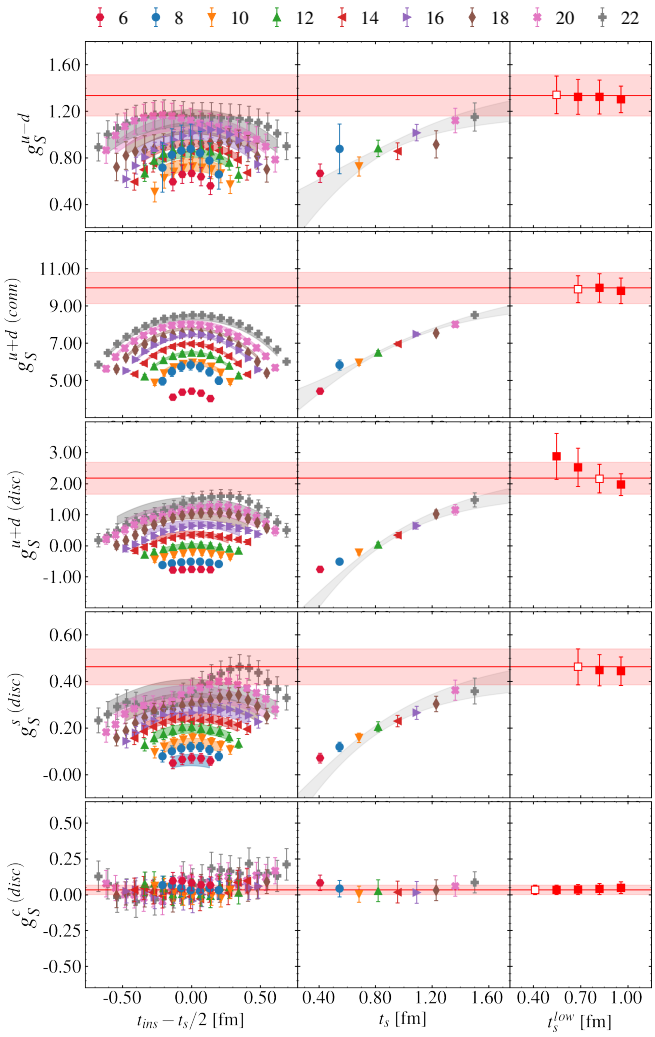

FIG. 7: The ratio and fit results for the C80 ensemble for scalar charges. The notation is the same as in Fig. 2 and the fits used for each charge are the same as in Fig. 6

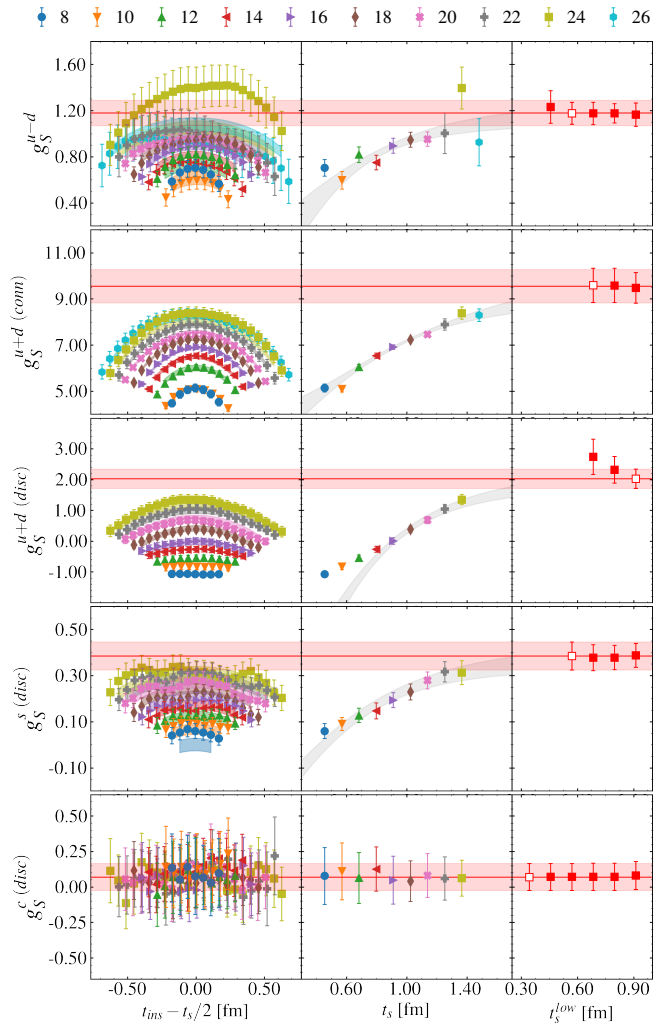

FIG. 8: The ratio and fit results for the D96 ensemble for scalar charges. The notation is the same as in Fig. 2 and the fits used for each charge are the same as in Fig. 6

The same analysis is carried out for the tensor charges, shown in Figs. 10, 11 and 12, where, similarly to the axial case, we observe excited state for the connected contributions but not for the disconnected. We thus perform 2-state fits for the connected and plateau fits for the disconnected. The continuum extrapolation in Fig. 13 follows the same procedure as for the axial and scalar cases presented so far. The values of the tensor charges are presented in Table VII.

g_T	$u-d$	$u+d$	$u+d-2s$	$u+d+s-3c$	$u+d+s+c$
B64	0.947(30)	0.531(21)	0.537(21)	0.533(21)	0.528(21)
C80	0.938(18)	0.545(14)	0.544(13)	0.547(14)	0.541(13)
D96	0.955(15)	0.557(19)	0.560(19)	0.563(20)	0.553(20)
$a=0$	0.955(29)	0.561(34)	0.561(33)	0.569(37)	0.557(34)

g_T	u	d	s	c
B64	0.739(23)	-0.207(11)	-0.00259(64)	-0.0012(17)
C80	0.741(14)	-0.1976(73)	-0.0004(12)	-0.0014(21)
D96	0.756(16)	-0.1989(72)	-0.00149(62)	-0.0027(16)
$a=0$	0.756(29)	-0.196(12)	-0.0009(11)	-0.0028(26)

TABLE VII: Values for the tensor 2-, 3-, and 4-flavor isovector and isoscalar combinations (top) and the extracted single flavor charges (bottom) for each ensemble and in the continuum limit.

B. Nucleon σ-terms

The nucleon σ-terms are defined as

$$\sigma^f = m_f \langle N|\bar{\psi}_f\psi_f|N\rangle \ , \quad \sigma^{u+d} = m_{ud} \langle N|\bar{u}u + \bar{d}d|N\rangle \, , \tag{23}$$

for a given quark ψ_f of flavor f, where m_f is the quark mass, or for the isoscalar combination with m_{ud} the average light quark mass and $|N\rangle$ the nucleon state. The value of σ^{u+d} or $\sigma^{\pi N}$ is also known from phenomenological analyses using input from experiment. These quantities are fundamental in QCD as they give the quark content of the nucleon and their values are a measure of

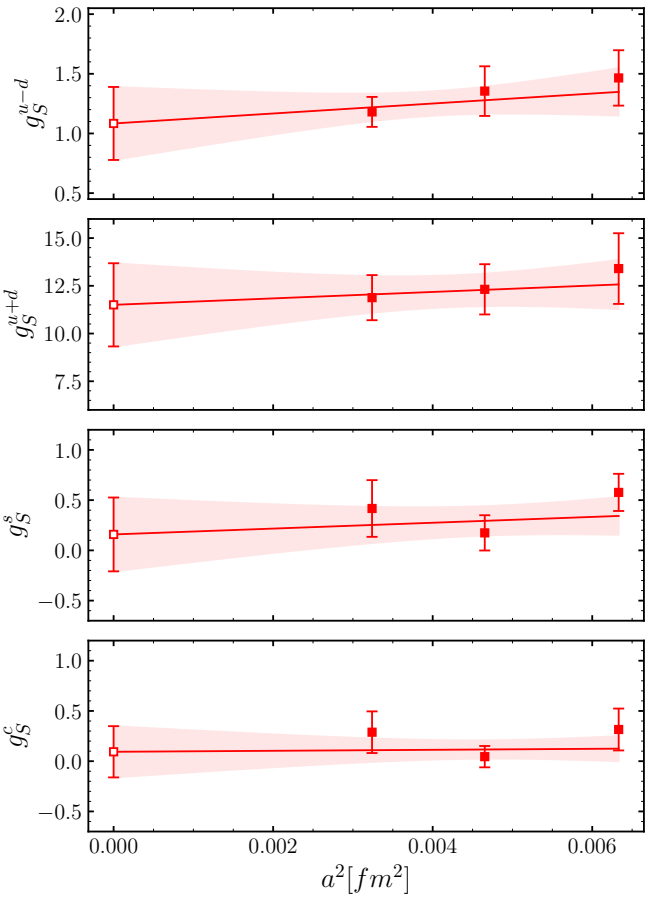

FIG. 9: Continuum limit of the nucleon scalar charges following the notation and procedure described in Fig. 5 for the axial case.

chiral symmetry breaking.

We extract the nucleon σ-terms, using the matrix elements of the scalar operator directly, including the disconnected quark loops. In the twisted mass formulation the renormalization is simpler compared to standard Wilson, since there is no additive mass renormalization for the quark masses and the multiplicative renormalization of the scalar current and of the quark mass cancel. Our results for $\sigma^{\pi N}$, σ^s and σ^c are given in Table VIII.

	$\sigma^{\pi N}$	σ^s	σ^c
B64	50.1(7.2)	56(12)	126(43)
C80	47.4(4.8)	45.4(7.6)	43(41)
D96	43.7(3.6)	37.5(6.0)	80(110)
$a = 0$	41.9(8.1)	30(17)	82(29)

TABLE VIII: Results for the nucleon σ-terms for each ensemble and in the continuum. For $\sigma_{\pi N}$ and for σ_s we follow the same extrapolation procedure as described in Fig. 5, while for σ_c we use a single constant extrapolation.

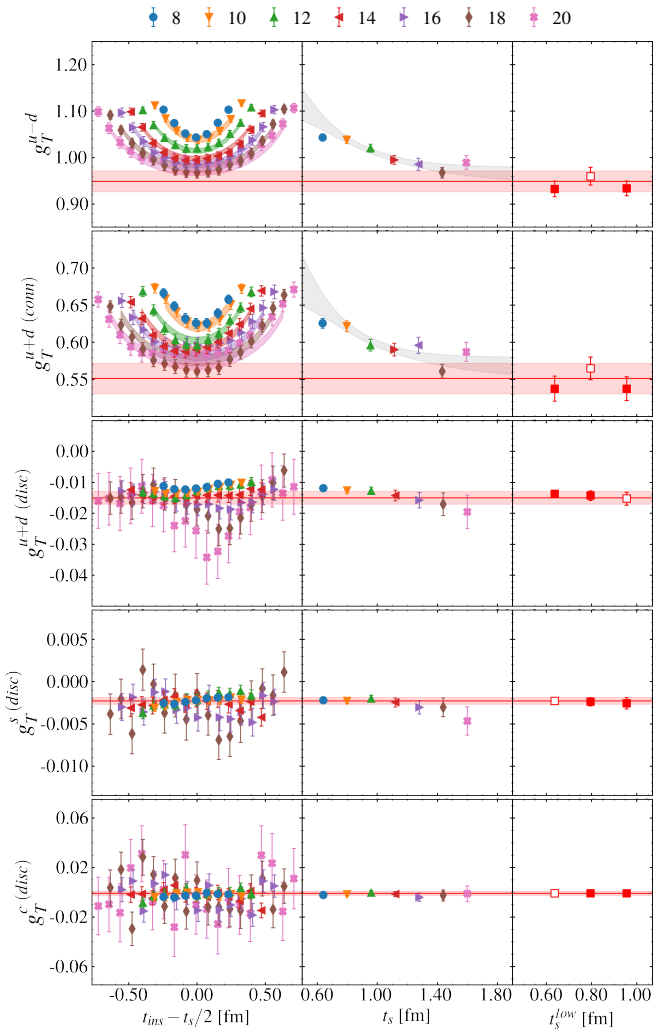

FIG. 10: The ratio and fit results for the B64 ensemble for tensor charges. The notation is the same as in Fig. 2.

C. Comparison with other results

In this section we compare our results with recent results from other lattice QCD studies as well as from phenomenology. We first comment on previous analyses of these quantities by ETMC:

- In Ref. [38], a comprehensive study of the nucleon isovector axial and pseudoscalar form factors is performed using the same three ensemble analyzed here, including a systematic error analysis. The final result for the isovector axial charge is obtained using only a single linear extrapolation compared to the model average strategy used in this work. We denote this result by ETM23 in Fig. 14.

- In Ref. [39], the isovector tensor charge was extracted using the same three ensembles analyzed here. In this work, we increase statistics for the B64 ensemble and for the two-point functions for the D96 ensemble. We also implement the AIC for extracting our final result. We denote this result

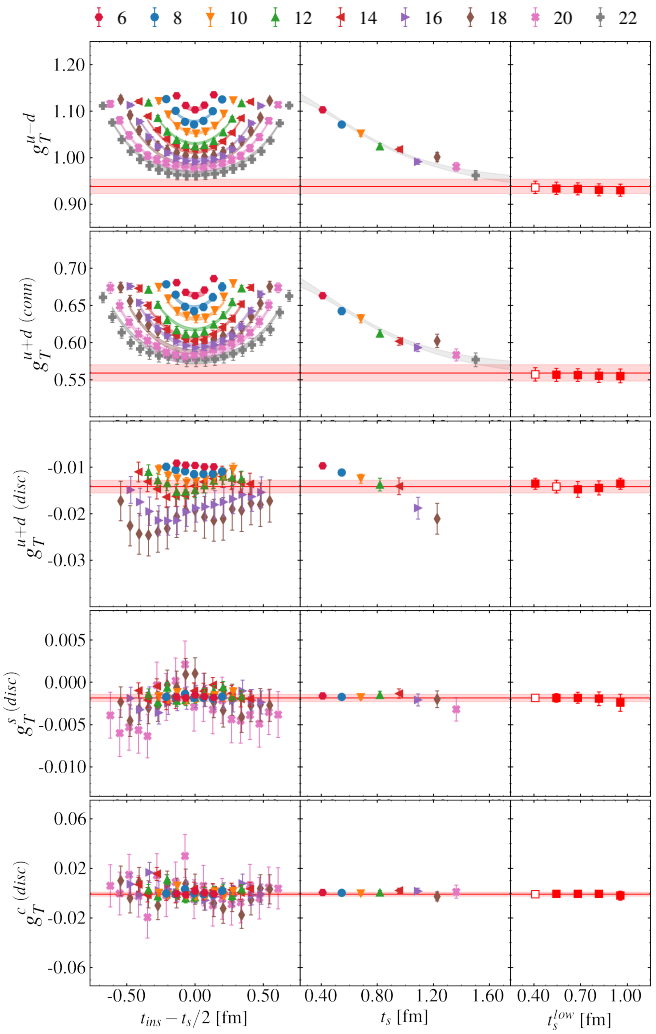

FIG. 11: The ratio and fit results for the C80 ensemble for tensor charges. The notation is the same as in Fig. 2.

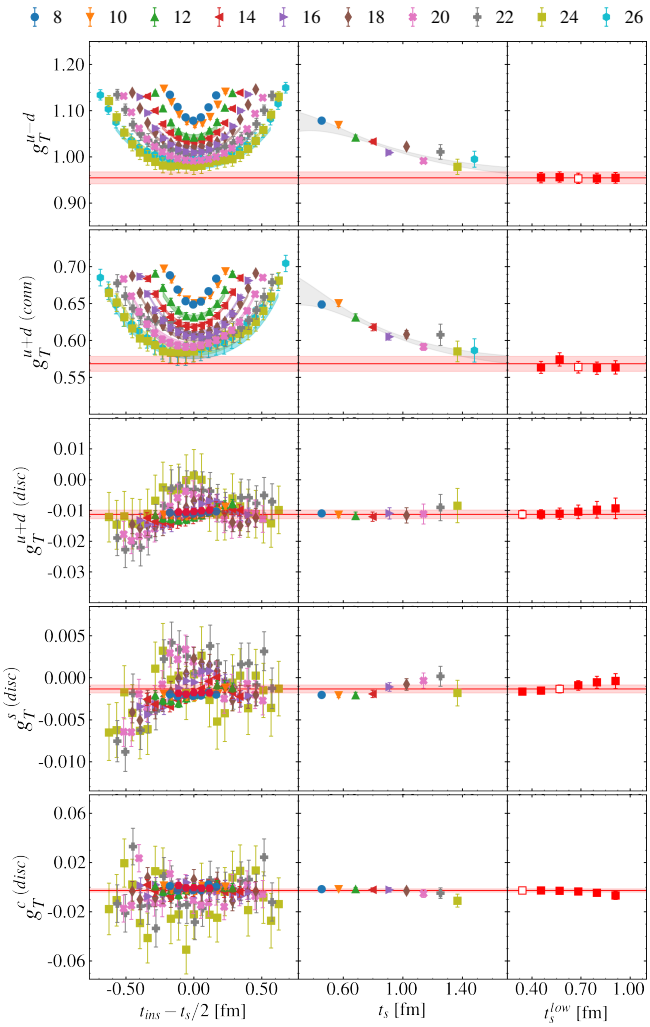

FIG. 12: The the ratio and fit results for the D96 ensemble for tensor charges. The notation is the same as in Fig. 2.

by ETM22 in Fig. 14.

- In Ref. [40], an analysis of the same quantities presented here was carried out for the B64 ensemble, the only ensemble of the three available at the time. Thus, those results were obtained without a continuum limit extrapolation and in addition no model averaging was performed. We denote these results by ETM19 in Figs. 14-17.

Comparing among ETMC results, we observe that for the isovector axial charge g_A^{u-d} shown in Fig. 14, ETMC values are consistent and the errors are approximately the same after taking the continuum limit. For the isovector scalar charge g_S^{u-d}, we observe an increase in the error due to the continuum extrapolation. For the isovector tensor charge g_T^{u-d}, there is only a slight increase in the error compared to the one obtained using only the B64 gauge ensemble. However, the current improved analysis yields a smaller error as compared to our previous analysis using the same three ensembles and taking the continuum limit.

We also compare our results with those from other collaborations, noting that the results presented here are the only ones obtained with the continuum limit taken using ensembles simulated directly at the physical pion mass. In contrast, all collaborations to which we compare to here rely either exclusively on ensembles simulated with heavier-than-physical pion masses or combining one or two physical point ensembles with heavier-than-physical ensembles. Since results at the physical point carry larger statistical uncertainties in general, their extrapolations may be weighted more heavily by data from the heavier-than-physical ensembles rather than from their physical point simulations. Given that chiral extrapolations for nucleon quantities are less reliable compared to the meson sector [59], this approach may introduce unaccounted systematic errors, which our work avoids by not requiring such extrapolations.

In Figs. 14, 15 and 16 we compare our results for the nucleon charges with previous ETMC results and values from other collaborations and in Fig. 17 we provide a similar comparison for the πN, strange and charm σ-

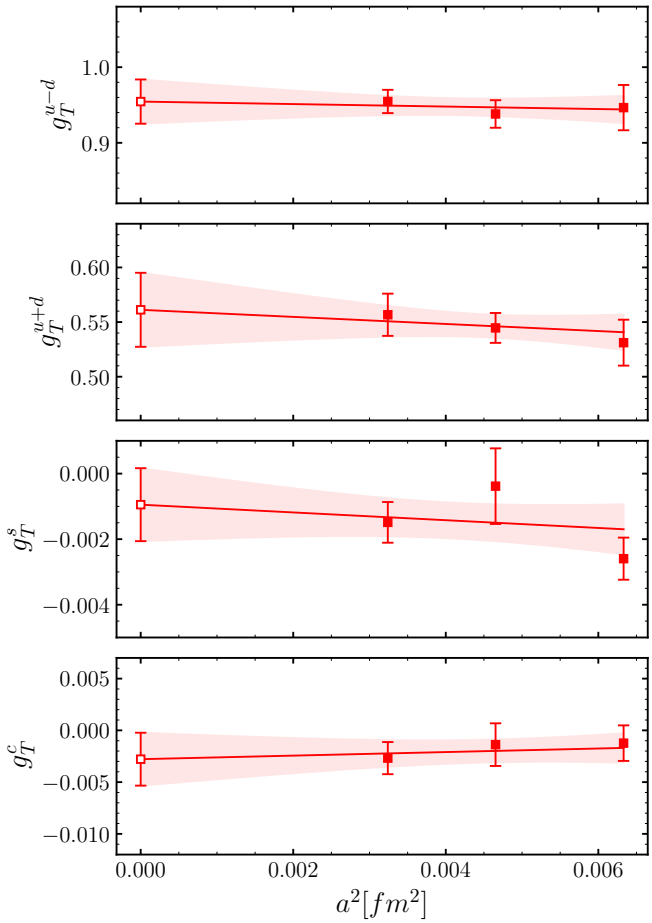

FIG. 13: Continuum limit of the nucleon tensor charges following the notation and procedure described in Fig. 5 for the axial case.

terms. Below we give some details on recent studies by other lattice QCD collaborations on the nucleon charges and σ-terms.

- The PNDME collaboration analyzed thirteen $N_f = 2+1+1$ ensembles of the MILC collaboration, simulated using highly improved staggered quarks (HISQ) in the sea, and using a mixed action approach whereby they use clover-improved valence quarks to compute the nucleon correlation functions. The gauge ensembles are at four lattice spacings, 0.06 fm, 0.09 fm, 0.12 fm and 0.15 fm, three pion masses (135 MeV, 220 MeV and 310 MeV), and volumes with $3.7 \leq m_\pi L \leq 5.5$. Two of these ensembles are at the physical pion mass. A combined continuum limit and chiral extrapolation was performed to extract the isovector nucleon charges. Their results are denoted as PNDME23 [42] in Fig. 14.

  The PNDME collaboration also extracted the up, down and strange axial and tensor charges [49] using the same setup as for the isovector charges and nine $N_f = 2+1+1$ ensembles with lattice spacings from 0.06 fm to 0.15 fm, pion masses from 136

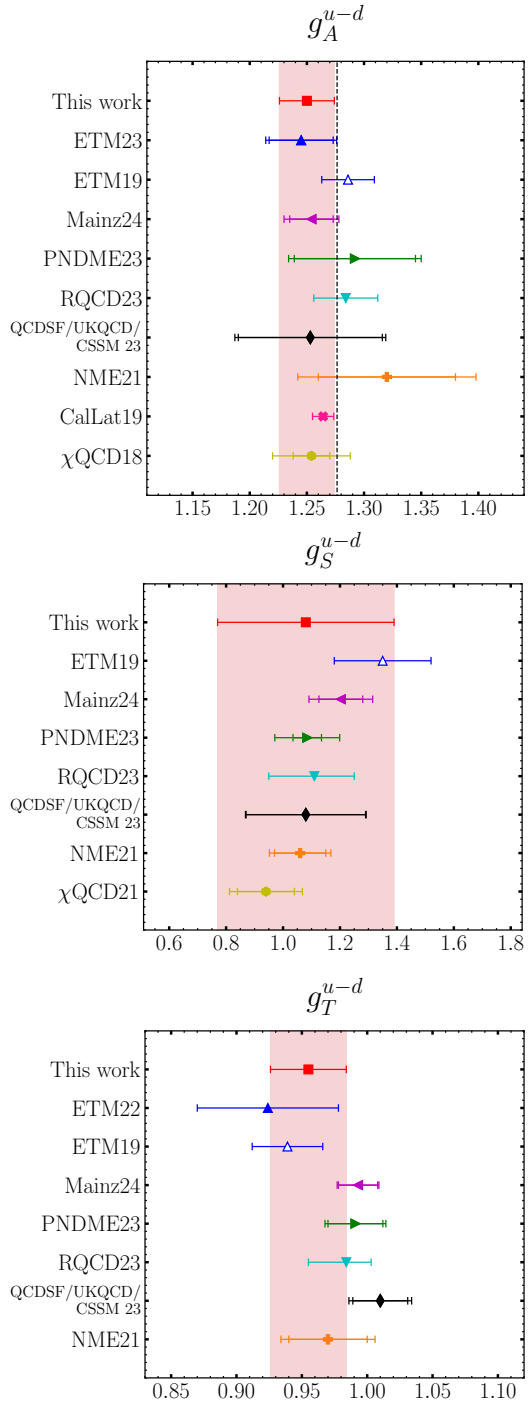

FIG. 14: Comparison of the results of this work with other lattice QCD results, for the isovector axial (top), scalar (center), and tensor (bottom) charges. Our results are shown with the red square and red error band. The blue triangles show previous ETMC results [38–40]. Open symbols represent results without a continuum limit extrapolation. The magenta triangles show recent results from the Mainz group [41], the green triangles from PNDME [42], the cyan triangles from RQCD [43], the black diamonds from the QCDSF/UKQCD/CSSM collaboration [44], the orange crosses from NME [45], the pink cross from CalLat [46] and the yellow hexagons from χQCD [47, 48]. For g_A^{u-d}, the dashed line represents the experimental value [37].

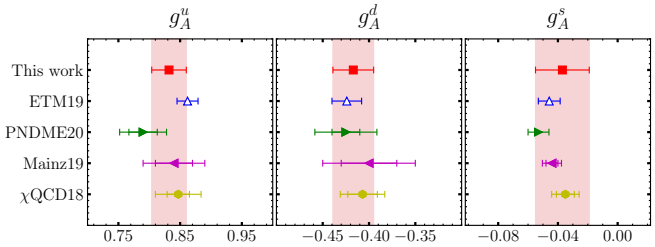

FIG. 15: Comparison of our results for the up- (left), down- (center), and strange-quark (right) contributions to the axial charge with other lattice QCD studies. Our results are shown with the red square and red error band. The blue triangles show previous ETMC results [40]. The green triangles show results from PNDME [49], the magenta triangles from the Mainz group [50] and the yellow hexagons from χQCD [47].

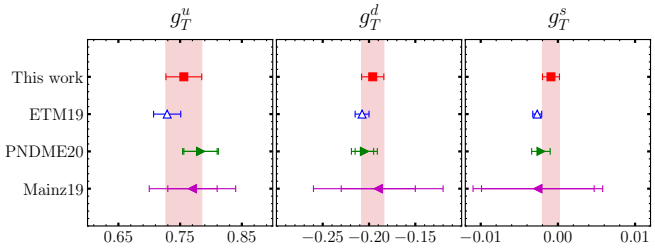

FIG. 16: Comparison of our results for the up- (left), down- (center), and strange-quark (right) contributions to the tensor charges with other lattice QCD analyses. Our results are shown with the red square and red error band. The blue triangles show previous ETMC results [40]. The green triangles show results from PNDME [49] and the magenta triangles from the Mainz group [50].

MeV to 320 MeV and volumes with $3.7 \leq m_\pi L \leq 4.79$. These results are denoted as PNDME20 in Figs. 15 and 16.

Furthermore, an evaluation of the $\sigma_{\pi N}$ was carried by PNDME [52] using six $N_f = 2+1+1$ ensembles at three lattice spacings, 0.12, 0.09, and 0.06 fm, three pion mass values, with one ensemble at 138 MeV and the remaining at 230 MeV and 315 MeV, and volumes with $3.90 \leq m_\pi L \leq 4.79$. Their quoted result, denoted by PNDME21 in Fig. 17, is obtained by explicitly treating $N\pi$ and $N\pi\pi$ excited states. This is motivated by chiral perturbation theory and brings their result in agreement with phenomenology.

- The RQCD collaboration performed an extensive study of nucleon charges and σ-terms [43] using forty-seven $N_f = 2+1$ clover-improved fermion ensembles mostly produced within the Coordinated Lattice Simulations (CLS) effort. These ensembles are simulated using pion masses spanning from 130 Mev to 430 MeV, with six lattice spacings between $a \approx 0.039 fm$ and $a \approx 0.098 fm$ and volumes with $3.0 \leq m_\pi L \leq 6.5$ with two of them having pion mass close to the physical value. They obtained their final values, denoted by RQCD23 in Figs. 14 and 17, after a simultaneous continuum and chiral extrapolation.

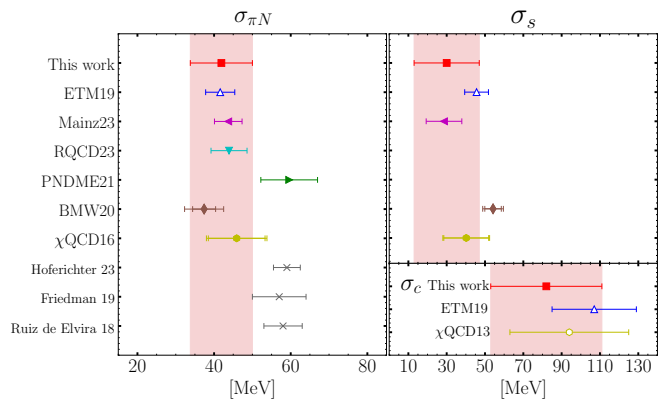

FIG. 17: Comparison of our results for the nucleon sigma terms with other lattice works and with results from phenomenology for $\sigma_{\pi N}$. Our results are shown with the red square and red error band. The blue triangles show previous ETMC results [40]. The magenta triangles show results from the Mainz group [51], the cyan triangles from RQCD [43], the green triangles from PNDME [52], the brown diamonds from BMW [53] and the yellow hexagons from χQCD [54, 55]. Open symbols represent results without a continuum limit extrapolation. Results from phenomenology as shown in grey crosses [56–58].

- The Mainz collaboration for their isovector charges results in Ref. [41] used fifteen $N_f = 2+1$ CLS ensembles with pion masses in the range of 130 MeV $\leq m_\pi \leq$ 360 MeV, four lattice spacings and volumes with $3.05 \leq m_\pi L \leq 5.89$. They performed continuum and chiral extrapolations, with one ensemble having a pion mass close to its physical value and one about 30 MeV above. Their results on the isovector charges are denoted by Mainz24 in Fig. 14. In addition, they computed the up, down and strange axial and tensor charges [50], using eight CLS $N_f = 2+1$ gauge ensembles, with four lattice spacings ranging from 0.050 fm to 0.086 fm and volumes with $3.78 \leq m_\pi L \leq 5.29$. In this analysis they have no physical point ensembles, using pion masses in the range 200 MeV-360 Mev. They carry out a combined fit to extrapolate to the continuum limit and to the physical pion mass obtaining the results denoted by Mainz19 in Figs. 15 and 16.

  To extract the $\sigma_{\pi N}$ and σ_s, sixteen CLS ensembles were analyzed with pion masses in the range 174 MeV $\leq m_\pi \leq$ 352 MeV, lattice spacings ranging from 0.050 fm to 0.086 fm and volumes with $3.00 \leq m_\pi L \leq 5.83$ [51]. Continuum and chiral extrapolations are performed. The results are denoted by Mainz23 in Fig. 17.

- The QCDSF/UKQCD/CSSM collaboration [44] used twenty-one $N_f = 2+1$ gauge ensembles, a tree-level Symanzik improved gluon action and nonperturbatively $\mathcal{O}(a)$ clover-improved Wilson fermions.

Their pion masses are in the range 220 MeV $\leq m_\pi \leq$ 468 MeV, with five lattice spacings and three lattice volumes. They performed continuum and chiral extrapolations to extract the isovector charges shown in Fig. 14.

- The NME collaboration, for their calculation of the isovector charges [45], used seven $N_f = 2+1$ clover-improved Wilson fermion ensembles. Their pion masses are in the range 166 MeV $\leq m_\pi \leq$ 285 MeV, with lattice spacings ranging from 0.071 fm to 0.127 fm and volumes with $3.75 \leq m_\pi L \leq 6.15$. Results are obtained after chiral and continuum limit extrapolations. These results are denoted as NME21 in Fig. 14.

- The CalLat collaboration computed g_A^{u-d} using an approach inspired by the Feynman-Hellmann Theorem [46, 60]. They use a hybrid setup of $N_f = 2+1+1$ HISQ staggered fermion in the sea generated by the MILC collaboration and domain-wall fermions as valence quarks. Sixteen gauge ensembles were analyzed, spanning three lattice spacings ($a \approx 0.15,\ 0.12,\ 0.09$ fm) and pion mass values in the range 130-400 MeV. The final value, denoted as CalLat19 in Fig. 14, is obtained after a simultaneous chiral and continuum extrapolation.

- The χQCD collaboration computed the isovector and the up, down and strange axial charges [47] using a hybrid setup of domain wall fermion sea and overlap valence quarks. They analyzed three RBC/UKQCD $N_f = 2+1$ gauge ensembles with three lattice spacings, $a = 0.08$ fm, $a = 0.11$ fm and $a = 0.14$ fm, two volumes and three pion masses 171 MeV, 302 MeV and 337 MeV. They performed continuum and chiral extrapolations and the results are denoted by χQCD18 in Figs. 14 and 15.

  The χQCD collaboration also computed g_S^{u-d}, denoted as χQCD21 in Fig. 14. They analyzed five RBC/UKQCD $Nf = 2+1$ domain-wall ensembles, with four lattice spacings, $a = 0.06, 0.08, 0.11, 0.14$ fm [48], one ensemble with physical pion mass and the rest with pion masses in the range 171 MeV to 371 MeV at three different volumes.

  For the calculation of the pion-nucleon and strange σ-terms [54], three RBC/UKQCD $Nf = 2+1$ domain-wall ensembles were used with lattice spacings, $a = 0.08$ fm and $a = 0.11$ fm, three pion masses, 139 MeV, 300 MeV and 330 Mev, and three different volumes. Their results on $\sigma_{\pi N}$ and σ_s are obtained after chiral and continuum extrapolations and are denoted by χQCD16 in Fig. 17. χQCD is the only collaboration, besides ETMC, that computed the charm σ-term by directly evaluating the charm quark loop. The calculation of σ_c [55] was done using only one ensemble with pion mass 331 MeV, volume $24^3 \times 64$ and $a = 0.11$fm. For all other quantities we only compare to other collaborations when the results are at the physical mass point and in the continuum limit. However, since this is the only other lattice QCD result on σ_c we include it in Fig. 17 denoted as χQCD13.

- The BMW collaboration used the Feynman-Hellmann relation based on the derivative of the nucleon mass with respect to the corresponding quark mass to determine $\sigma_{\pi N}$, σ_s and σ_c [53]. For that purpose, they used 33 $N_f = 1+1+1+1$ 3HEX-smeared, clover-improved Wilson ensembles with pion masses in the range of 195 MeV to 420 MeV, the strange and charm quark masses spanning their physical values, four lattice spacings in the range $0.06 - 0.10$ fm and spatial volumes $3.7 \leq m_\pi L \leq 12.2$. Their values for $\sigma_{\pi N}$ and σ_s, denoted as BMW20, are shown in Fig. 17. Their error on σ_c is very large and thus not included in the comparison.

In Fig. 14, where we show results for the isovector charges, we observe very good agreement among lattice QCD results by different collaborations for all isovector charges. Moreover, our value for the isovector axial charge g_A^{u-d}, is compatible with experimental measurements [37]. As can be seen in Fig. 15 and 16, there is a good agreement among lattice QCD results for the up, down, strange and charm axial and tensor charges.

In Fig. 17, where we collected results for the πN, strange and charm σ-terms we observe that for the isovector scalar charge, there is a significant error increase when taking the continuum limit as compared to our previous results using only the B64 gauge ensemble [40]. While there is an overall good agreement among lattice results, a tension of about two standard deviations is observed with the latest value from the PNDME collaboration [52], where the pion-nucleon contribution was explicitly included using chiral perturbation theory, yielding a value that is closer to phenomenological results. The BMW collaboration used a different method to extract the σ-terms computing the dependence of the nucleon mass on the quark masses. Their values agree with the ones extracted from the the computation of the nucleon three-point function where excited states may contribute differently, giving confidence on the proper extraction of the nucleon matrix element. Furthermore, in our recent study [61, 62], where we included the pion-nucleon interpolating fields in a generalized eigenvalue problem analysis, we found no detectable improvement. This indicates that the tension of lattice QCD results on $\sigma_{N\pi}$ with phenomenology has a different origin.

VI. CONCLUSIONS

We present results on the nucleon axial, scalar and tensor charges, as well as the nucleon σ-terms, using three $N_f = 2+1+1$ ensembles with twisted mass clover-improved fermions, with quark masses tuned to repro-

duce their physical values. This enables us, for the first time, to determine these charges and σ-terms at the continuum limit using only physical point ensembles, avoiding any chiral extrapolations.

We find for the isovector charges:

$$g_A^{u-d} = 1.250(24),\ g_S^{u-d} = 1.08(31),\ g_T^{u-d} = 0.955(29),$$

that are in agreement with results by other collaborations. The value we get for the isovector axial charge also agrees with the experimental value. The scalar and tensor isovector charges determined here can provide input for experimental efforts on scalar and tensor interactions for BSM physics searches.

We also use the scalar matrix element to extract the values of the σ-terms, that are of significant importance in the direct detection of dark matter. Our value $\sigma_{\pi N} = 41.9(8.1)$, is in agreement with most lattice results, but within approximately one standard deviation with phenomenological results that tend to give larger values.

The observed trend of increasing errors in several quantities, when taking the continuum limit, emphasizes the significance of utilizing more physical point ensembles preferably with smaller lattice spacings in taking the continuum limit. Our goal in the future is the inclusion of such an additional ensemble with a$\sim$ 0.05 for taking the continuum limit, increasing the accuracy in the final values.

ACKNOWLEDGMENTS

We thank all members of the ETM collaboration for a most conducive cooperation. C.A. and G. K. acknowledge partial support from the European Joint Doctorate AQTIVATE that received funding from the European Union's research and innovation programme under the Marie Sklodowska-Curie Doctoral Networks action under the Grant Agreement No 101072344. Y.L. is supported by the Excellence Hub project "Unraveling the 3D parton structure of the nucleon with lattice QCD (3D-nucleon)" id EXCELLENCE/0421/0043 co-financed by the European Regional Development Fund and the Republic of Cyprus through the Research and Innovation Foundation and by funding provided by the University of Cyprus through the project "Nucleon generalized parton distributions within lattice QCD (Nucleon-GPDs)". Ch. I. is supported by the project Nucleon-GPDs. S. B. and G. K. acknowledge support by the Excellence Hub project "NiceQuarks" id EXCELLENCE/0421/0195 co-financed by the European Regional Development Fund S.B. and J.F. acknowledge financial support from the Inno4scale project, which received funding from the European High-Performance Computing Joint Undertaking (JU) under Grant Agreement No. 101118139. The JU receives support from the European Union's Horizon Europe Programme. J.F. received support by the DFG research unit FOR5269 "Future methods for studying confined gluons in QCD" and acknowledges financial support by the Next Generation Triggers project (https://nextgentriggers.web.cern.ch).

The open-source packages tmLQCD [63–66], LEMON [67], DD-αAMG [68–71], QPhiX [72, 73] and QUDA [74–76] have been used in the ensemble generation. The open-source software PLEGMA has been used for the analyais.

The authors gratefully acknowledge the Gauss Centre for Supercomputing e.V. (www.gauss-centre.eu) for providing computing time on the GCS Supercomputers SuperMUC-NG at Leibniz Supercomputing Centre, JUWELS [77] and JUWELS Booster [78] at Juelich Supercomputing Centre (JSC). Part of the results were created within the EA program of JUWELS Booster also with the help of the JUWELS Booster Project Team (JSC, Atos, ParTec, NVIDIA). We acknowledge the Swiss National Supercomputing Centre (CSCS) and the EuroHPC Joint Undertaking for awarding this project access to the LUMI supercomputer, owned by the EuroHPC Joint Undertaking, hosted by CSC (Finland) and the LUMI consortium through the Chronos programme under project IDs CH16-CYP. We are grateful to CINECA and the EuroHPC JU for awarding access to supercomputing facilities hosted at CINECA and to Leonardo-Booster, provided to us through the Extreme Scale Access Call grant EHPC-EXT-2024E01-027. The authors also acknowledge computing time granted on Cyclone at the Cyprus institute (CyI) via the project with ids P061, P146 and pro22a10951.

[1] T. Bhattacharya, V. Cirigliano, S. D. Cohen, A. Filipuzzi, M. Gonzalez-Alonso, M. L. Graesser, R. Gupta, and H.-W. Lin, Phys. Rev. **D85**, 054512 (2012), 1110.6448.

[2] I. Bischer and W. Rodejohann, Phys. Rev. D **99**, 036006 (2019), 1810.02220.

[3] D. Akimov et al. (COHERENT), Science **357**, 1123 (2017), 1708.01294.

[4] A. Beda, V. Brudanin, V. Egorov, D. Medvedev, V. Pogosov, M. Shirchenko, and A. Starostin, Adv. High Energy Phys. **2012**, 350150 (2012).

[5] T. Marrodán Undagoitia and L. Rauch, J. Phys. G **43**, 013001 (2016), 1509.08767.

[6] M. V. Chizhov, Phys. Lett. B **381**, 359 (1996), hep-ph/9511287.

[7] L. Dhargyal, Springer Proc. Phys. **203**, 329 (2018), 1610.06293.

[8] C. Cocuzza, A. Metz, D. Pitonyak, A. Prokudin, N. Sato, and R. Seidl (JAM), Phys. Rev. Lett. **132**, 091901 (2024), 2306.12998.

[9] R. Frezzotti, P. A. Grassi, S. Sint, and P. Weisz (Alpha), JHEP **08**, 058 (2001), hep-lat/0101001.
[10] R. Frezzotti and G. C. Rossi, JHEP **08**, 007 (2004), hep-lat/0306014.
[11] B. Sheikholeslami and R. Wohlert, Nucl. Phys. **B259**, 572 (1985).
[12] C. Alexandrou et al. (Extended Twisted Mass), Phys. Rev. D **107**, 074506 (2023), 2206.15084.
[13] C. Alexandrou et al., Phys. Rev. **D98**, 054518 (2018), 1807.00495.
[14] J. Finkenrath et al., PoS **LATTICE2021**, 284 (2022), 2201.02551.
[15] C. Alexandrou et al. (Extended Twisted Mass), Phys. Rev. D **104**, 074515 (2021), 2104.13408.
[16] C. McNeile and C. Michael (UKQCD), Phys. Rev. **D73**, 074506 (2006), hep-lat/0603007.
[17] A. S. Gambhir, A. Stathopoulos, and K. Orginos, SIAM J. Sci. Comput. **39**, A532 (2017), 1603.05988.
[18] A. Stathopoulos, J. Laeuchli, and K. Orginos (2013), 1302.4018.
[19] A. Abdel-Rehim, C. Alexandrou, M. Constantinou, J. Finkenrath, K. Hadjiyiannakou, K. Jansen, C. Kallidonis, G. Koutsou, A. V. Avilés-Casco, and J. Volmer, PoS **LATTICE2016**, 155 (2016), 1611.03802.
[20] C. Alexandrou, S. Gusken, F. Jegerlehner, K. Schilling, and R. Sommer, Nucl. Phys. **B414**, 815 (1994), hep-lat/9211042.
[21] S. Gusken, Nucl. Phys. Proc. Suppl. **17**, 361 (1990).
[22] C. Alexandrou, S. Bacchio, M. Constantinou, J. Finkenrath, K. Hadjiyiannakou, K. Jansen, G. Koutsou, and A. V. A. Casco (2018), 1812.10311.
[23] C. Alexandrou et al. (2019), 1908.10706.
[24] M. Albanese et al. (APE), Phys. Lett. **B192**, 163 (1987).
[25] W. I. Jay and E. T. Neil, Phys. Rev. D **103**, 114502 (2021), 2008.01069.
[26] E. T. Neil and J. W. Sitison, Phys. Rev. D **109**, 014510 (2024), 2208.14983.
[27] G. Martinelli, C. Pittori, C. T. Sachrajda, M. Testa, and A. Vladikas, Nucl. Phys. **B445**, 81 (1995), hep-lat/9411010.
[28] M. Gockeler, R. Horsley, H. Oelrich, H. Perlt, D. Petters, P. E. Rakow, A. Schafer, G. Schierholz, and A. Schiller, Nucl. Phys. B **544**, 699 (1999), hep-lat/9807044.
[29] C. Alexandrou, M. Constantinou, and H. Panagopoulos (ETM), Phys. Rev. **D95**, 034505 (2017), 1509.00213.
[30] K. G. Chetyrkin, Phys. Lett. B **404**, 161 (1997), hep-ph/9703278.
[31] J. A. Gracey, Nucl. Phys. B **662**, 247 (2003), hep-ph/0304113.
[32] J. A. Gracey, Phys. Rev. D **106**, 085008 (2022), 2208.14527.
[33] M. Constantinou, M. Hadjiantonis, H. Panagopoulos, and G. Spanoudes, Phys. Rev. **D94**, 114513 (2016), 1610.06744.
[34] S. A. Larin, Phys. Lett. B **303**, 113 (1993), hep-ph/9302240.
[35] O. Bär, Phys. Rev. D **99**, 054506 (2019), 1812.09191.
[36] O. Bär, Phys. Rev. D **94**, 054505 (2016), 1606.09385.
[37] B. Märkisch et al., Phys. Rev. Lett. **122**, 242501 (2019), 1812.04666.
[38] C. Alexandrou, S. Bacchio, M. Constantinou, J. Finkenrath, R. Frezzotti, B. Kostrzewa, G. Koutsou, G. Spanoudes, and C. Urbach (Extended Twisted Mass), Phys. Rev. D **109**, 034503 (2024), 2309.05774.
[39] C. Alexandrou et al., Phys. Rev. D **107**, 054504 (2023), 2202.09871.
[40] C. Alexandrou, S. Bacchio, M. Constantinou, J. Finkenrath, K. Hadjiyiannakou, K. Jansen, G. Koutsou, and A. Vaquero Aviles-Casco, Phys. Rev. D **102**, 054517 (2020), 1909.00485.
[41] D. Djukanovic, G. von Hippel, H. B. Meyer, K. Ottnad, and H. Wittig, Phys. Rev. D **109**, 074507 (2024), 2402.03024.
[42] Y.-C. Jang, R. Gupta, T. Bhattacharya, B. Yoon, and H.-W. Lin (Precision Neutron Decay Matrix Elements (PNDME)), Phys. Rev. D **109**, 014503 (2024), 2305.11330.
[43] G. S. Bali, S. Collins, S. Heybrock, M. Löffler, R. Rödl, W. Söldner, and S. Weishäupl (RQCD), Phys. Rev. D **108**, 034512 (2023), 2305.04717.
[44] R. E. Smail et al. (QCDSF/UKQCD/CSSM), Phys. Rev. D **108**, 094511 (2023), 2304.02866.
[45] S. Park, R. Gupta, B. Yoon, S. Mondal, T. Bhattacharya, Y.-C. Jang, B. Joó, and F. Winter (Nucleon Matrix Elements (NME)), Phys. Rev. D **105**, 054505 (2022), 2103.05599.
[46] A. Walker-Loud et al., PoS **CD2018**, 020 (2020), 1912.08321.
[47] J. Liang, Y.-B. Yang, T. Draper, M. Gong, and K.-F. Liu, Phys. Rev. D **98**, 074505 (2018), 1806.08366.
[48] L. Liu, T. Chen, T. Draper, J. Liang, K.-F. Liu, G. Wang, and Y.-B. Yang (χQCD), Phys. Rev. D **104**, 094503 (2021), 2103.12933.
[49] S. Park, T. Bhattacharya, R. Gupta, Y.-C. Jang, B. Joo, H.-W. Lin, and B. Yoon, PoS **LATTICE2019**, 136 (2020), 2002.02147.
[50] D. Djukanovic, H. Meyer, K. Ottnad, G. von Hippel, J. Wilhelm, and H. Wittig, PoS **LATTICE2019**, 158 (2019), 1911.01177.
[51] A. Agadjanov, D. Djukanovic, G. von Hippel, H. B. Meyer, K. Ottnad, and H. Wittig, Phys. Rev. Lett. **131**, 261902 (2023), 2303.08741.
[52] R. Gupta, S. Park, M. Hoferichter, E. Mereghetti, B. Yoon, and T. Bhattacharya, Phys. Rev. Lett. **127**, 242002 (2021), 2105.12095.
[53] S. Borsanyi, Z. Fodor, C. Hoelbling, L. Lellouch, K. K. Szabo, C. Torrero, and L. Varnhorst (2020), 2007.03319.
[54] Y.-B. Yang, A. Alexandru, T. Draper, J. Liang, and K.-F. Liu (xQCD), Phys. Rev. D **94**, 054503 (2016), 1511.09089.
[55] M. Gong et al. (XQCD), Phys. Rev. D **88**, 014503 (2013), 1304.1194.
[56] E. Friedman and A. Gal, Phys. Lett. **B792**, 340 (2019), 1901.03130.
[57] J. Ruiz de Elvira, M. Hoferichter, B. Kubis, and U.-G. Meißner, J. Phys. **G45**, 024001 (2018), 1706.01465.
[58] M. Hoferichter, J. R. de Elvira, B. Kubis, and U.-G. Meißner, Phys. Lett. B **843**, 138001 (2023), 2305.07045.
[59] P. E. Shanahan, J. Phys. G **43**, 124001 (2016), 1606.08812.
[60] C. C. Chang et al., Nature **558**, 91 (2018), 1805.12130.
[61] C. Alexandrou, G. Koutsou, Y. Li, M. Petschlies, and F. Pittler, Phys. Rev. D **110**, 094514 (2024), 2408.03893.
[62] C. Alexandrou, G. Koutsou, Y. Li, M. Petschlies, and F. Pittler, PoS **LATTICE2023**, 080 (2024), 2312.15737.
[63] K. Jansen and C. Urbach, Comput. Phys. Commun. **180**, 2717 (2009), 0905.3331.
[64] A. Abdel-Rehim, F. Burger, A. Deuzeman, K. Jansen,

B. Kostrzewa, L. Scorzato, and C. Urbach, PoS **LATTICE2013**, 414 (2014), 1311.5495.

[65] A. Deuzeman, K. Jansen, B. Kostrzewa, and C. Urbach, PoS **LATTICE2013**, 416 (2014), 1311.4521.

[66] B. Kostrzewa, S. Bacchio, J. Finkenrath, M. Garofalo, F. Pittler, S. Romiti, and C. Urbach (ETM), PoS **LATTICE2022**, 340 (2023), 2212.06635.

[67] A. Deuzeman, S. Reker, and C. Urbach (ETM), Comput. Phys. Commun. **183**, 1321 (2012), 1106.4177.

[68] A. Frommer, K. Kahl, S. Krieg, B. Leder, and M. Rottmann, SIAM J. Sci. Comput. **36**, A1581 (2014), 1303.1377.

[69] C. Alexandrou, S. Bacchio, J. Finkenrath, A. Frommer, K. Kahl, and M. Rottmann, Phys. Rev. D **94**, 114509 (2016), 1610.02370.

[70] S. Bacchio, C. Alexandrou, and J. Finkerath, EPJ Web Conf. **175**, 02002 (2018), 1710.06198.

[71] C. Alexandrou, S. Bacchio, and J. Finkenrath, Comput. Phys. Commun. **236**, 51 (2019), 1805.09584.

[72] B. Joó, D. D. Kalamkar, T. Kurth, K. Vaidyanathan, and A. Walden, pp. 415–427 (2016).

[73] M. Schröck, S. Simula, and A. Strelchenko, PoS **LATTICE2015**, 030 (2016), 1510.08879.

[74] M. A. Clark, R. Babich, K. Barros, R. C. Brower, and C. Rebbi, Comput. Phys. Commun. **181**, 1517 (2010), 0911.3191.

[75] R. Babich, M. A. Clark, B. Joo, G. Shi, R. C. Brower, and S. Gottlieb (2011), 1109.2935.

[76] M. A. Clark, B. Joó, A. Strelchenko, M. Cheng, A. Gambhir, and R. C. Brower, pp. 795–806 (2016), 1612.07873.

[77] Jülich Supercomputing Centre, Journal of large-scale research facilities **5** (2019), URL `http://dx.doi.org/10.17815/jlsrf-5-171`.

[78] Jülich Supercomputing Centre, Journal of large-scale research facilities **7** (2021), URL `http://dx.doi.org/10.17815/jlsrf-7-183`.